Ocean Science
Discussions

Please see my annotations.

The life cycle of submesoscale eddies generated by topographic interactions

Mathieu Morvan[1], Pierre L'Hégaret[1], Xavier Carton[1], Jonathan Gula[1], Clément Vic[2],
Mikhail Sokolovskiy[3], and Konstantin Koshel[4]

[1]LOPS, Univ. Brest-CNRS-IFREMER-IRD, IUEM
[2]National Oceanographic Center, University of Southampton, European Way, Southampton, SO14 3ZH, UK
[3]Institute of Water Problems of the RAS, Ul Gubkina 3, Moscow, 199333, Russia, Shirshov Institute of Oceanology of RAS, 36 Nahimovskiy pr., Moscow, 117997, Russia
[4]V.I.Il'ichev Pacific Oceanological Institute, 43, Baltiyskaya Street, Vladivostok, 690041, Russia

Correspondence: Mathieu Morvan (mmorvan3@univ-brest.fr)

Abstract.

The Persian Gulf Water and Red Sea Water are salty and dense waters recirculating at subsurface in the Gulf of Oman and the Gulf of Aden respectively, under the influence of mesoscale eddies which dominate the surface flow in both semi-enclosed basins. In situ measurements combined with altimetry indicate that the Persian Gulf Water is driven by mesoscale eddies in the form of filaments and submesoscale structures. In this paper, we study the formation and the life cycle of intense submesoscale vortices and their impact on the spread of Persian Gulf Water and Red Sea Water. We use a three-dimensional hydrostatic model with submesoscale-resolving resolution to study the evolution of submesoscale vortices. Our configuration is an idealized version of the Gulf of Oman and Aden: a zonal row of mesoscale vortices interacting with north and south topographic slopes. Intense submesoscale vortices are generated in the simulations along the continental slopes due to two different mechanisms. The first mechanism is due to frictional generation of vorticity in the bottom boundary layer, which detaches from the topography, forms an unstable vorticity filament, and undergoes horizontal shear instability that leads to the formation of submesoscale coherent vortices. The second mechanism is inviscid and implies arrested topographic Rossby waves breaking and forming submesoscale coherent vortices where a mesoscale anticyclone interacts with the topographic slope. Submesoscale vortices subsequently drift away, merge and form larger vortices. They can also pair with opposite signed vortices and travel across the domain. They can weaken or disappear via several mechanisms, in particular fusion into the larger eddies or erosion on the topography. Particle patches are advected and sheared by vortices and are entrained into filaments. Their size first grows as the square root of time, a signature of the merging processes, then it increases linearly with time, corresponding to their ballistic advection by submesoscale eddies. On the contrary, witout intense submesoscale eddies, particles are mainly advected by mesoscale eddies; this implies a weaker dispersion of particles than in the previous case. This shows the important role of submesoscale eddies in spreading Persian Gulf Water and Red Sea Water.

1 Introduction

Mesoscale eddies $[\mathcal{O}(10\text{-}100)\text{km}]$ are ubiquitous in the world's oceans. The mesoscale eddy field dominates the energy content of oceanic currents at sub-inertial frequencies and is crucial to large-scale budgets of heat and geochemical tracers. Although their generation mechanisms are clearly identified and quantified, largely stemming from large-scale current instabilities, how

5   they dissipate their energy remains unclear (Ferrari and Wunsch, 2009). The interaction of these mesoscale vortices can lead to the formation of smaller scale features (Carton, 2001). Submesoscale eddies $[\mathcal{O}(1\text{-}10)\text{km}]$ can be generated as the result of frontal instabilities (Capet et al., 2008a, b, c) feeding off the energy of the mesoscale currents. Recently, numerical models highlighted one possible mechanism for mesoscale energy dissipation, which is the interaction of mesoscale eddies with the underlying seafloor topography (Molemaker et al., 2015; Gula et al., 2015, 2016; Vic et al., 2015). This specific interaction

10   also leads to the formation of submesoscale eddies. In this regime, the influence of stratification is still important, but the Coriolis force is less prevalent in the horizontal momentum budgets (viz. the Rossby number of the flow is not always small; McWilliams (2016)). Submesoscale eddies have been sampled for decades, yet their lifecycle (from generation to dissipation) is poorly understood (McWilliams, 1985; D'Asaro, 1988; Bosse et al., 2015).

15   The Arabian Sea is home to an energetic mesoscale eddy field (Carton et al., 2012; Vic et al., 2014; L'Hégaret et al., 2015). In particular, they can interact with the salty and dense waters of the outflows from the Persian Gulf and from the Red Sea (Bower et al., 2002; Al Saafani et al., 2007). These salty and dense waters flow out of these seas into the Gulf of Oman and into the Gulf of Aden and settle at 250-300 m and 600-1000 m depths, respectively (Pous et al., 2004a; Bower and Furey, 2012). These two gulfs also receive Rossby and Kelvin waves, and vortices, propagating westwards from the Arabian Sea (L'Hégaret

20   et al., 2013). Mesoscale vortices divert the outflow paths away from the coast, advect them along curved trajectories around the eddy rims, elongate these outflows as salty filaments and finally, can break these filaments into small eddies (Pous et al., 2004b; Carton et al., 2012). The chaotic dispersion of a tracer by a mesoscale vortex row in a realistic numerical simulation of the Japan Sea has previously been studied by Prants et al. (2011). However, the details of the spreading mechanism, involving submesoscale eddies, has not been explored.

25

    In this paper, we focus on the life cycle of the submesoscale eddies generated by mesoscale eddy-topography interactions, combining observational data from dedicated campaigns and numerical simulations specifically designed to resemble the local geography of the Gulf of Aden and the Gulf of Oman. Vic et al. (2015) studied the case of a mesoscale dipole along a continental shelf, reminiscent of the situation described in L'Hégaret et al. (2013). But satellite observations during the spring

30   inter-monsoon and the summer monsoon reveal the presence of vortex rows with alternate polarities in the Gulf of Aden and in the Gulf of Oman. A vortex row is more efficient than a single dipole to form small eddies, but it is also more prone to destroying them by shearing and stretching effects. These mechanisms will be studied here. We further quantify how these submesoscale eddies participate in the spreading of the dense overflow waters modelled here as a passive tracer. We compare and analyze a

[handwritten annotations: "this is not true. modify this statement", "ing", "(because the geometry used in this study is very idealized.)"]

set of three numerical experiments for which submesoscale eddies are not necessarily formed.

The data and numerical model used in this study are presented in Section 2. Observations of submesoscale eddies and frag-
ments formed from the Persian Gulf Water outflow in the Gulf of Oman in spring 2014 are presented in Section 3.1. Then,
5   generation and life-cycle of the submesoscale eddies due to the interaction of a vortex row with continental slopes is analysed
using idealized numerical simulations in sections 3.2, 3.3 and 3.4.

2   Material and methods

2.1   The Physindien 2011 campaign

10   The Physindien experiment was carried out in spring 2011 to study the Persian Gulf Water outflow current in the Gulf of
Oman, and to monitor the eddies there and south of the Arabian Peninsula. The Beautemps-Beaupre research vessel deployed
a CTD/ADCP (Conductivity Temperature and Depth probe/Acoustic Doppler Current Profiler) probe at different positions, to
record vertical profiles of pressure, salinity, temperature and currents; it also towed a Seasoar, a platform carrying two CTD's,
undulating between 0 and 350 m depths behind the ship. The measurement accuracies after processing and validation on other
15   (independent) sensors were $10^{-3}\,^{\circ}\text{C}, 5\,10^{-3}\,\text{psu}$. The horizontal velocity was obtained with a $38\,\text{kHz}$ ship-mounted ADCP;
this device measures currents from the surface to about 1000 m depth; the depth range depends on the matter in suspension in
seawater, which can reflect the acoustic signal. The accuracy of the horizontal components of velocity is $5 \times 10^{-3}\,\text{m}\,\text{s}^{-1}$. The
characteristics of the Persian Gulf Water are highlighted *via* the vertical sections of temperature, salinity and density.

2.2   Numerical set up

20   To investigate the origin and the dynamics of submesoscale vortices, we set up idealized simulations of a row of four mesoscale
surface intensified vortices with alternate polarities, in a zonally periodic channel, by using the Coastal and Regional Ocean
COmmunity (CROCO) model at submesoscale-resolving resolution on a f-plane.

The CROCO model is a primitive equation model solving the hydrostatic Boussinesq Navier Stokes equations with Coriolis
25   acceleration due to the Earth rotation. The extent of the channel is $[600\,\text{km}; 200\,\text{km}; 2000\,\text{m}]$ in the x-,y- and z-directions re-
spectively. The horizontal grid spacing is $1\,\text{km}$. On the vertical, 100 submesoscale-resolving σ-levels stretched at the bottom
are used.

The mean stratification is chosen such that the deformation radius is about 40 km, as computed by Chelton et al. (1998) for
30   this region. The mean vertical profile of temperature is

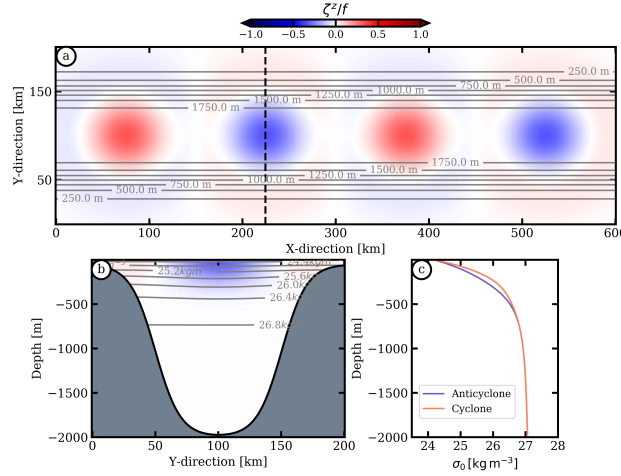$$T(z) = T_0 \exp(z/H), \tag{1}$$

Figure 1. Initial state: (a) Vertical relative vorticity (normalized by the Coriolis frequency) for the four mesoscale surface intensified eddies. Black contours are the isobaths. (b) Vertical cross-section of an anticyclone. (c) Vertical profiles of density associated with the cores of a mesoscale cyclone (orange) and of an anticyclone (blue).

where $T_0 = 28\,°\mathrm{C}$ and $H = 2000\,\mathrm{m}$ (mean depth of the Gulf of Oman). T_0 is chosen so that the surface density field is representative of the Gulf of Oman. The salinity is kept to $35\,\mathrm{psu}$ over the water column.

We initialize the flow with four mesoscale vortices, with alternate polarity along the channel axis (Figure 1). The radial and vertical profiles of circular velocity of each vortex are :

$$v_\theta\left(r,z\right) = \pm \frac{v_0 r}{R} \exp\left(-\frac{r^2}{R^2}\right) \exp\left(-\frac{z^2}{D^2}\right), \tag{2}$$

with $v_0 = 0.5\,\mathrm{rad\,s^{-1}}$, $R = 50\,\mathrm{km}$, $D = 300\,\mathrm{m}$. Then the velocity field of the four mesoscale eddies is balanced with their pressure field using the cyclo-geostrophic equilibrium and following the procedure described in Ciani et al. (2016). The density anomalies associated with the vortices are directly computed using the hydrostatic equilibrium. The vortices are separated from each other horizontally by $150\,\mathrm{km}$. The distance between the vortex cores and the northern and southern edges is $100\,\mathrm{km}$.

To characterize the impact of the frictional effects at the bottom and of the topography shape on the submesoscale eddy generation, we design three experiments with different bottom boundary conditions (with or without bottom drag and bottom boundary layer) and with different topographies (with or without a cape). In the first experiment (EXP1), we use a free slip bottom boundary condition with no bottom boundary layer mixing and parameterize the smooth bathymetry representative of the continental slope in the Gulf of Oman as:

$$h = h_{shelf} + \frac{1}{2}\left(H - h_{shelf}\right)\left(\tanh\left(\frac{y - y^*}{W_y}\right) - \tanh\left(\frac{y - y_N}{W_y}\right)\right), \tag{3}$$

where $h_{shelf} = 100\,\mathrm{m}$, $H = 2000\,\mathrm{m}$, $y^* = y_S = 50\,\mathrm{km}$, $y_N = L_y - y_S$, $L_y = 200\,\mathrm{km}$ and $W_y = 20\,\mathrm{km}$.

In the second experiment (EXP2), the same bathymetry is used but we add a bottom drag and a vertical mixing at the bottom with a KPP scheme (Large et al., 1994). The bottom drag is implementend *via* the Von-Karman quadratic bottom stress formulation defined as:

$$\tau_{\mathbf{b}} = \rho_0 C_D \parallel \mathbf{u} \parallel \mathbf{u}, \tag{4}$$

where ρ_0 is a reference density. C_D is the drag coefficient varying as:

$$C_D = \left(\frac{\kappa}{\log\left(\Delta z_b / z_r\right)} \right)^2, \tag{5}$$

where κ is the Von-Karman constant equal to 0.41, z_r is the roughness parameter equal to $1\,\mathrm{cm}$ and Δz_b is the thickness of the lowest layer of the grid. These parametrizations lead to the formation of a turbulent bottom boundary layer (BBL hereafter) as soon as a current flows over a sloping bottom topography.

Then, in the third experiment (EXP3), we add a cape in the topography defined by eq. 3 by setting $y^* = y_S + y_0 \exp\left(-\left(\frac{x-x_0}{W_x}\right)^2\right)$, $y_0 = 40\,\mathrm{km}$ and $W_x = 20\,\mathrm{km}$. We use the same parametrizations of the vertical mixing at the bottom and the bottom drag as EXP2.

Finally, we use the ARIANE tool (Blanke and Raynaud, 1997) to study the impact of the production of submesoscale eddies on the spread of Lagrangian particles from the coast towards the center of the gulf. The Persian Gulf outflow Water is not explicitly included in the model and thus Lagrangian particles are used to model this water mass. ARIANE is a computational tool dedicated to the offline calculation of 3D streamlines in the output velocity field of model whose equations are based on volume conservation. Transports of water masses or currents are deduced from the displacement of numerical Lagrangian particles.

3 Submesoscale eddy life cycle

3.1 Observations in the Physindien 2011 in-situ data

In spring 2011, a vortex row of alternate polarity was present along the axis of the Gulf of Oman. The Persian Gulf Water (PGW) outflow was present along the continental slope of Oman (south of the Gulf of Oman). The vortex row in the Gulf of Oman extracted small fragments from the PGW outflow. The Physindien 2011 Seasoar section crossed the outflow and the PGW fragments (see Figure 2a).

In particular sections GO13 and GO16 (see Figure 2b,c), show filaments of warm and salty water extending from the continental slope offshore over 50 and $60\,\mathrm{km}$ respectively. These filaments have a temperature above $21\,^\circ\mathrm{C}$ and a salinity reaching
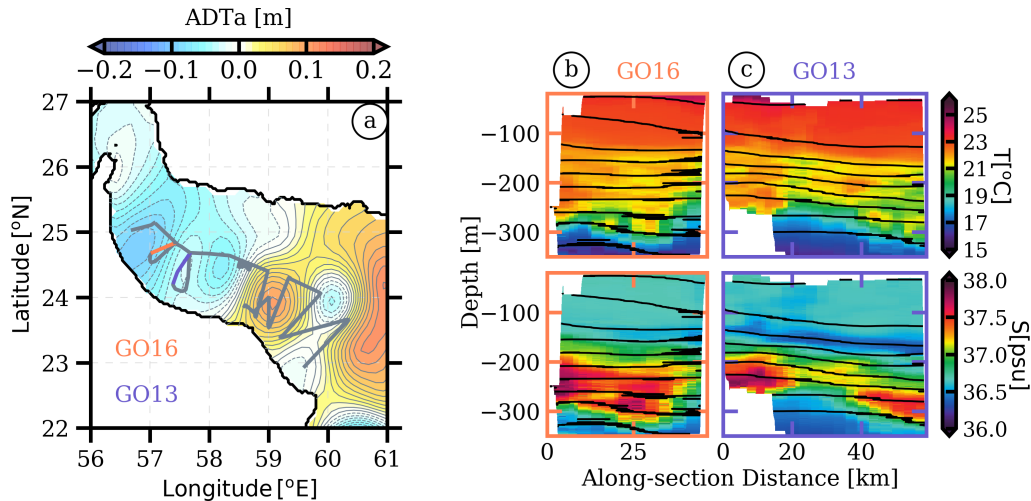
GO13 is hard to see in (2a).

Figure 2. a) Map of the Absolute Dynamic Topography anomalies in the Gulf of Oman averaged over the duration of the cruise processed by CLS-Argos on a $1/8^\circ$ Mercator grid. The solid grey lines indicate the locations of the Seasoar sections. The solid orange and blue lines stand for the sections GO16 and GO13 respectively. b-c) Temperature (top) and salinity (bottom) vertical sections of GO16 and GO13 sections respectively showing the warm and salty PGW outflow settled down to about $250\,\mathrm{m}$ depth in the Gulf of Oman.

What would be the effect of

← geometry vs. $\frac{f}{f}$

$37.5\,\mathrm{psu}$, characteristic of the PGW outflow at this location (L'Hégaret et al., 2015).

Both filaments are located between a cyclone (West) and an anticyclone (East). The PGW is advected offshore by the surface intensified mesoscale eddy. In the filaments, the structure is more complex, with an alternation of more or less salty water. This suggests that filaments could break into small vortices as they are advected by surface intensified mesoscale eddies.

3.2 Production of submesoscale eddies in the simulations

Numerous submesoscale vortices are generated in the numerical simulations. They are essentially found below $100\,\mathrm{m}$ depth, which corresponds to the depth of the shelf break. Submesoscale vortices originate from the interaction of mesoscale eddies with the sloping topography. In Figure 3, we show the relative vorticity field normalized by the Coriolis frequency at day 200 for the three numerical experiments near the surface, at 200 and $500\,\mathrm{m}$ depth. The surface flow is dominated by mesoscale eddies for all experiments. At $200\,\mathrm{m}$ depth, submesoscale filaments and vortices are visible around mesoscale eddies. They are more numerous and intense in the experiments in which both the bottom KPP and the bottom drag were active (i.e.: EXP2 and EXP3). This indicates that most of these submesoscale vortices are generated by bottom frictional effects. The absolute value of the relative vorticity associated with the submesoscale vortices is close to the planetary vorticity ($|\zeta^z/f| \sim 1$). The flow is dominated by an energetic submesoscale turbulence at $500\,\mathrm{m}$ for all experiments. Submesoscale filaments and vortices are also

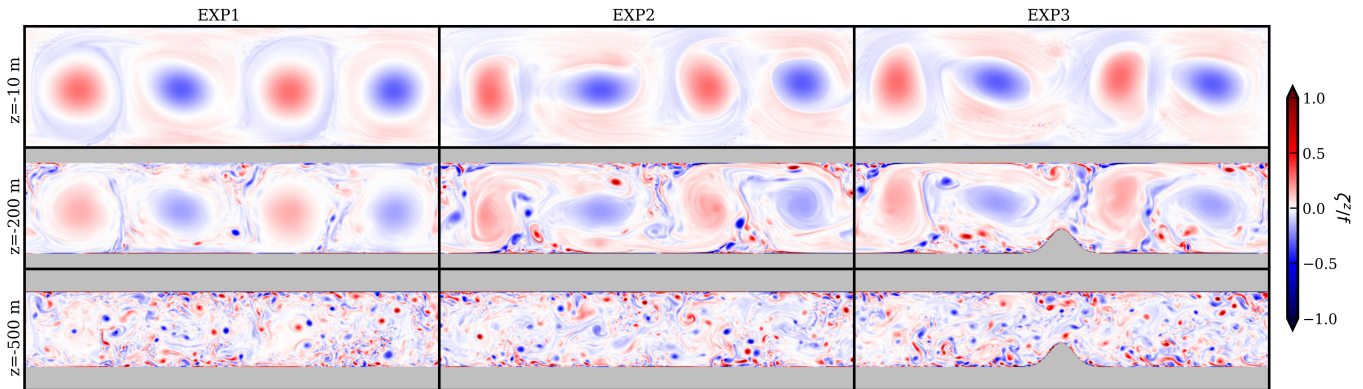Ocean Science
Discussions

Open Access

Figure 3. Vertical relative vorticity field normalized by the Coriolis frequency at day 200 and 10, 200 and 500 meter depth for EXP1, EXP2 and EXP3.

generated in EXP1, where there are no frictional effects at the bottom. This suggests that another mechanism leading to the production of small vortices is at play. This inviscid mechanism is related to the breaking of Topographic Rossby waves. It will be presented in Section 3.3.

In Figure 4, we compare the Power Spectrum Density of horizontal velocities for the three experiments (EXP1, EXP2 and
5 EXP3).

Consistently with the previous results, we observe a net increase of the kinetic energy below the Rossby deformation radius (R_d) below the surface for all simulations. This increase is actually the signature of subsurface submesoscale eddies. In the two simulations with bottom KPP and bottom drag (i.e.: EXP2 and EXP3), and in accordance with Vic et al. (2015), the part of the kinetic energy contained at the submesoscale is larger at 200 m. Near the surface, we observe a slight increase of the kinetic
10 energy below the Rossby deformation radius due to the surface signature of the subsurface submesoscale eddies.

Below $500\,\mathrm{m}$ depth, the shapes and the slopes of the spectra are similar for the 3 experiments. The flatter k^{-2} slope between 100 and $10\,\mathrm{km}$ of horizontal scale indicated an active submesoscale turbulence field and a submesoscale source of energy at around $10\,\mathrm{km}$.

3.3 Processes of submesoscale eddy generation

15 As mentioned in the previous section, two mechanisms implying eddy/topography interaction, leading to the formation of small vortices are at play.
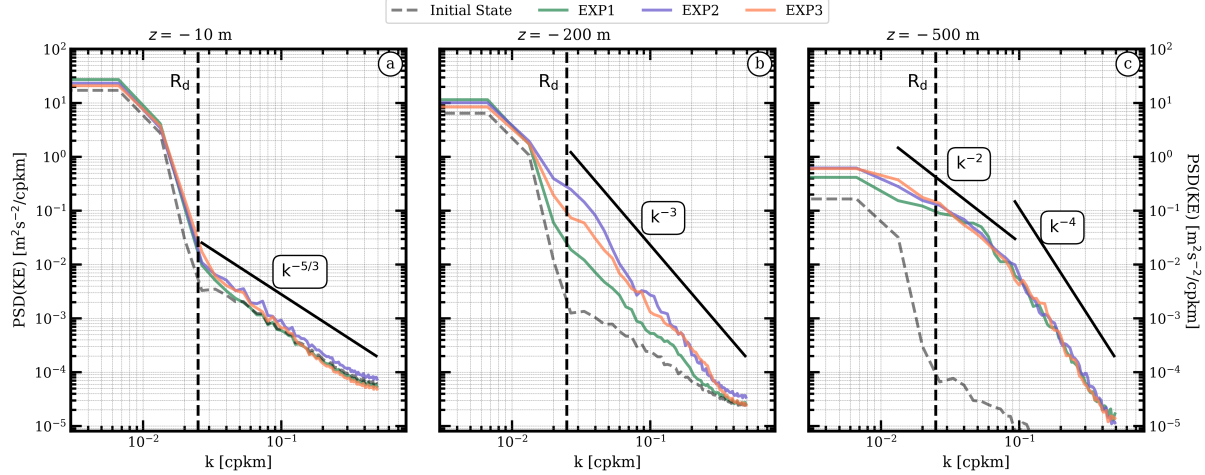
Ocean Science
Discussions

Figure 4. Kinetic Energy (KE) spectra comparison of the three experiments: EXP1 (green), EXP2 (blue), EXP3 (orange). Spectra are computed at (a) 10, (b) 200 and (c) 500 meter depth at day 200. Black lines stand for benchmarks of power laws.

3.3.1 Unstable Topographic Rossby Waves

The first mechanism is an inviscid mechanism visible below $300\,\mathrm{m}$ in all experiments. This mechanism is related to the breaking of Topographic Rossby waves (TRW hereafter). TRW are triggered by the eddy velocity fields acting as the perturbation along the sloping bathymetry. This can be seen in EXP1, in the absence of frictional effects. In Figure 5d, we show the Hovmöller diagram of the potential vorticity anomaly at $500\,\mathrm{m}$ depth near the southern boundary of the domain. The potential vorticity anomaly is diagnosed and computed as:

$$Q' = Q - Q_{rest}, \tag{6}$$

with

$$Q_{rest} = f_0 \partial_z \overline{b}, \tag{7}$$

where $\overline{b}$ is the background vertical stratification and,

$$Q = (f_0 + \partial_x v - \partial_y u)\partial_z b - \partial_z v \partial_x b + \partial_z u \partial_y b \,, \tag{8}$$

the Ertel Potential Vorticity.

The solid blue line in Figure 5a indicates that the phase speed is about $0.02\,\mathrm{m\,s^{-1}}$. We compare this value with that obtained considering the propagation of TRW in a homogeneous fluid. As defined in Cushman-Roisin and Beckers (2011), the dispersion
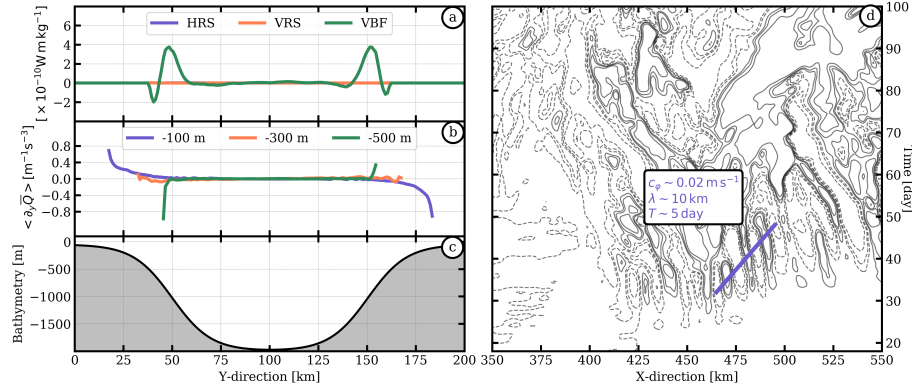
Ocean Science
Discussions

Figure 5. Diagnostics computed from EXP1. (a) Energy conversion terms: (blue) HRS, (orange) VRS and (green) VBF vertically integrated between 150 and 1000 m depth. (b) Timely and zonally averaged meridionnal PV gradient computed at (blue) 100, (orange) 300 and (green) 500 m depth. (c) Bathymetry. (d) Hovmoller diagram of potential vorticity anomaly at 500 m depth.

relation of TRW in a homogeneous fluid leads to the following expression for the phase speed:

$$c_\varphi = \frac{\alpha_0 g}{f_0} \frac{1}{1 + \frac{gH}{f_0^2}k^2}.$$ (9)

With $\alpha_0 = 0.15$, $g = 9.81\,\mathrm{m\,s^{-2}}$, $f_0 = 6 \times 10^{-5}\,\mathrm{s^{-1}}$, $H = 1500\,\mathrm{m}$ and $\lambda = \frac{2\pi}{k} = 10\,\mathrm{km}$ (measured in Figure 5d), we obtain $c_\varphi \sim 0.02\,\mathrm{m\,s^{-1}}$.

5   The TRW destabilizes below 300 m leading to the formation of submesoscale eddies. In Figure 5a, we show that TRW are baroclinically unstable over the sloping topography.

We characterize the instabilities by computing the energy transfer terms (Gula et al., 2016), i.e.: the Horizontal Reynolds Stress (HRS), the Vertical Reynolds Stress (VRS) and the Vertical Buoyancy Flux (VBF) as:

$$HRS = -\overline{\mathbf{u}'v'} \cdot \partial_t \overline{\mathbf{u}} - \overline{\mathbf{u}'u'} \cdot \partial_x \overline{\mathbf{u}};$$ (10)

10

$$VRS = -\overline{\mathbf{u}'w'} \cdot \partial_z \overline{\mathbf{u}};$$ (11)

$$VBF = \overline{w'b'};$$ (12)

where $\bullet'$ denote the deviation from the time average, $\overline{\bullet}$ the time average, $\mathbf{u}$ the horizontal velocity, w the vertical velocity and

15    $b = -g\frac{\rho}{\rho_0}$ the buoyancy.

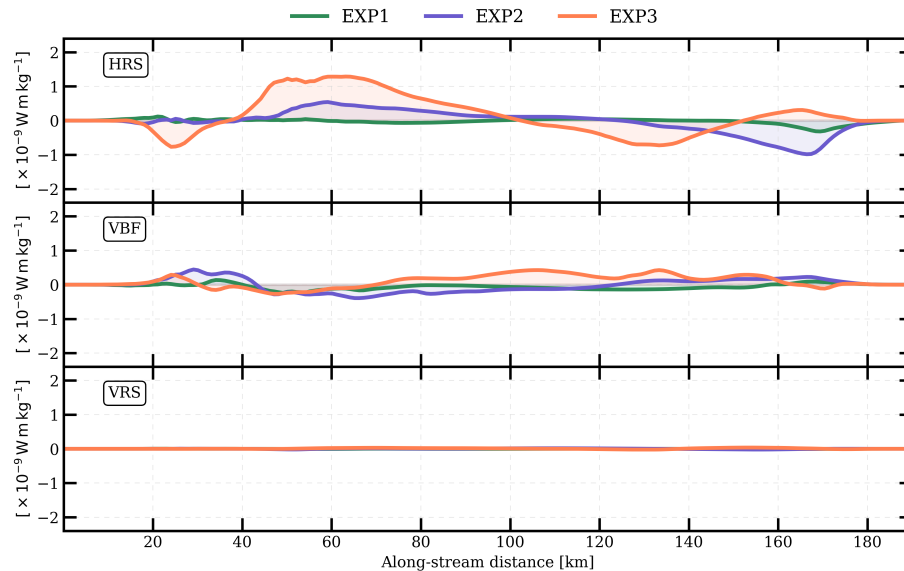Ocean Science
Discussions

Open Access

Figure 6. (Top) Horizontal Reynolds Stress, (Mid.) Vertical Reynolds Stress and (Bot.) Vertical Buoyancy Flux integrated between 100 and 300 m depth in the along-filament direction.

Locally, the vertical buoyancy flux is maximum over the sloping topography. There, the bathymetry is about 300 m depth. Indeed, it corresponds to the depth where the PV gradient sign change occurs. The PV gradient sign change originate from the sloping topography. In the upper part of the water column, the meridional gradient of PV is positive while it is negative in the lower part (see Figure 5b). This is a necessary condition for the baroclinic instability. The TRW propagate eastwards

5   over the southern sloping topography and westwards over the northern one. So, over the sloping topography, TRW propagate in the same direction as the velocity field associated with the mesoscale cyclones. On the contrary, TRW propagate in the opposite direction of the current associated with mesoscale anticyclones. The TRW can be arrested and destabilizes when the velocity of the flow is opposite to its phase speed. This can happen only when the TRW encounters a mesoscale anticyclone.

10   **3.3.2   Frictional layer detachment**

As mesoscale eddies drag over the sloping topography, they intensify the velocity shear within the bottom boundary layer (BBL hereafter) leading to a topographic vorticity generation forming filament-like structures. This BBL vorticity is directly linked with the use of a bottom drag and the bottom KPP and is possible only in EXP2 and EXP3. Subsequently, detached vorticity filaments become unstable under the influence of horizontal shear. In Figure 6, it clearly appears that horizontal shear instabili-

15   ties extract kinetic energy from the mean flow through the Horizontal Reynolds Stress ($HRS \gg VBF \gg VRS$). Barotropic instability is important near the topographic slope. Consequently, filaments roll-up into small eddies. This also means that
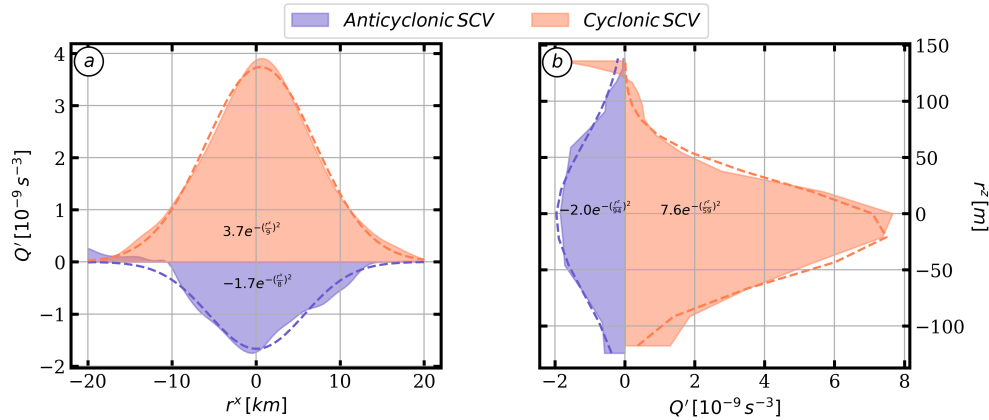
10

Figure 7. (a) Horizontal and (b) vertical profiles of potential vorticity anomaly associated with two SCVs.

kinetic energy is transferred from larger to smaller scales. Since the bottom boundary layer is regularly destabilized, small eddies are produced regularly by this frictional mechanism at each coast. When these eddies form and detach from the coast, they adjust cyclogeostrophically.

3.4 Structure and Lifecycle of the submesoscale eddies

In this section, we focus on the submesoscale eddies produced by BBL vorticity generation as the spatial scale and dynamical structure are in accordance with that found *via* the *in situ* measurement analysis.

Figure 7 shows the horizontal (a) and vertical (b) structures of such submesoscale eddies found between 100 and 300 m depths in EXP2.

The submesoscale eddies are typically about 20 km wide and 150 m thick. The structure of the submesoscale eddies produced throughout the mesoscale eddy/topography interaction is consistent with the structure observed ~~thanks to the~~ in the *in situ* measurements. The fits of the horizontal and vertical profiles of PV anomaly, are close to Gaussian in both directions. The absence of sign reversal of the PV gradient is a clue to the stability of these small eddies (in the absence of external flow), thus their potentially long time life. Indeed, the ambient shear strain imposed by mesoscale eddy field is about $5\,10^{-6}\,\mathrm{s}^{-1}$. It corresponds to $\sim 10\% \times \zeta_{SCV}$ which is close to the quasi-geostrophic value necessary for vortices to elongate irreversibly.

Submesoscale eddies are either cyclonic or anticyclonic, opposite to the polarity of their parent mesoscale eddy. In this paragraph, we describe the lifecycle of two submesoscale eddies: a cyclone and an anticyclone (see Figure 8 and 9). This lifecycle is typical of the submesoscale eddies observed in the model simulations, generated in the BBL by interaction of the mesoscale eddies with the topography. Once formed, the submesoscale eddies rapidly merge with their neighbors (see Figure 9b, from
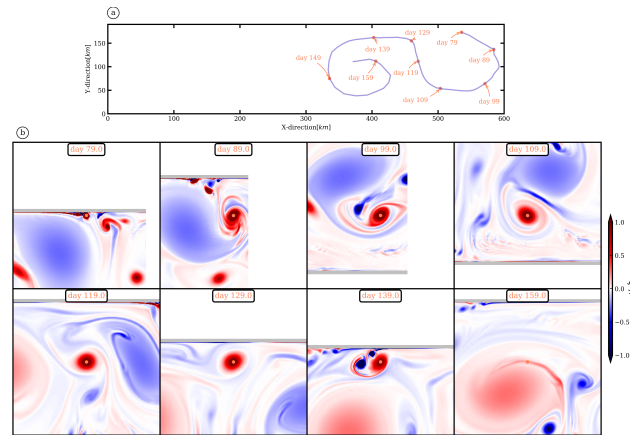
Figure 8. (a) Pathway of a submesoscale cyclone originates from the bottom boundary layer. (b) Major events from the birth till the death of the small vortex.

day 17 to 49). The inverse energy cascade associated with the merging events tends to set larger scales than the BBL-scale energy injection scale. This process allows them to grow and provisionally, to withstand destruction induced by the mesoscale velocity shear. While they grow, they are also advected offshore *via* a dipolar coupling with their parent mesoscale eddy. Thus, they grow to a diameter of 15-20 km, comparable with that shown in Figure 2b. At this stage, their radius is still smaller than

5 the deformation radius and $|\zeta^z/f| \geq 1$; they are Submesoscale Coherent Vortices (SCVs ; McWilliams (1985)).

In turn, as these vortices encounter the topographic slope, even smaller, opposite-signed vortices are produced (see Figure 8b at day 139 and Figure 9b at day 97); this leads to a slight dissipation of their energy. Then, the initial SCVs couple with the new opposite-signed SCVs, propagate again, and become strained and deformed. They are also sheared by the large vortices

10 and thus they decay in intensity (see for instance Figure 9b day 113). All these processes, generation of smaller vortices at the slope and vorticity erosion, contribute to feed the small scales in the enstrophy spectra.

The final evolution differs for the two SCVs. The cyclonic SCV merges with a mesoscale cyclone. The very details of this vortex interaction may not be fully captured by this hydrostatic model. A higher resolution, nonhydrostatic model would be

15 necessary to capture all the details of this small-scale vortex merger.[1] The anticyclonic SCV becomes less energetic after traveling over a long distance, and finally, it interacts again with the sloping topography. There, it looses most of its energy and disappears.

Depending on the number of merging events, on their distance to the mesoscale eddies and on their interaction with the sloping topography, the SCVs lifetimes vary between 10 and 100 days and the distance that they cover is at most 600 km. The global

20 trajectory of these small eddies is essentially governed by the mesoscale flow. But their life cycle and the major events affecting

---

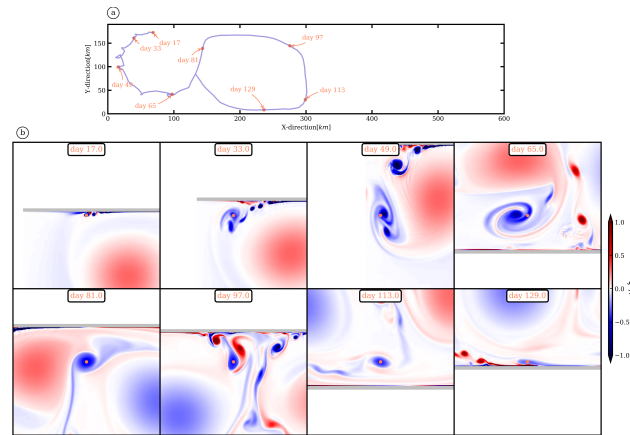[1]This will be the subject of a forthcoming study.

Figure 9. (a) Pathway of a submesoscale anticyclone originates from the bottom boundary layer. (b) Major events from the birth till the death of the small vortex.

them crucially depend on the population of submesoscale eddies and on the interaction with topography.

3.5 Spreading of outflow waters

We examine the capability of the submesoscale vortices to carry a tracer, such as the anomalously high salt content associated with the Persian Gulf Water and the Red Sea Water. To do so, we release about 10,000 particles into the two SCVs of Figures 8 and 9, at their birth (i.e. at day 79 for the cyclone and at day 17 for the anticyclone).

In Figure 10 we show the mean squared distance between particles and their center of mass ($< D^2(t) >$) *vs* the age of particles. The results exhibit two regimes. The first regime is associated with a fairly linear trend of the RMS distance with time. For short times, a dispersion coefficient κ can be found *via* :

$$< D^2(t) >= 4\kappa t,$$ (13)

as proposed by LaCasce and Bower (2000). The

ave 377 and 188 m²/s,

Calculations yield 377 and 188m²s⁻¹ as diffusivities for the cyclonic and the anticyclonic SCVs respectively. Our estimate corresponds to the dispersion associated with the SCV merging events. During this period, the SCVs lose only a few particles compared to the second regime. This second regime exhibits an enhanced growth of particle loss. This stage corresponds to the dipolar advection of submesoscale eddies coupled with their mesoscale neighbor. This regime is characterized as ballistic since $< D^2(t) >\propto t^2$.

Through time, we calculate the number of particles located within 8 km of each submesoscale eddy. In Figure 11a, we show the trajectories of submesoscale eddies in solid lines and the positions of selected particles with dots. The time evolution of the
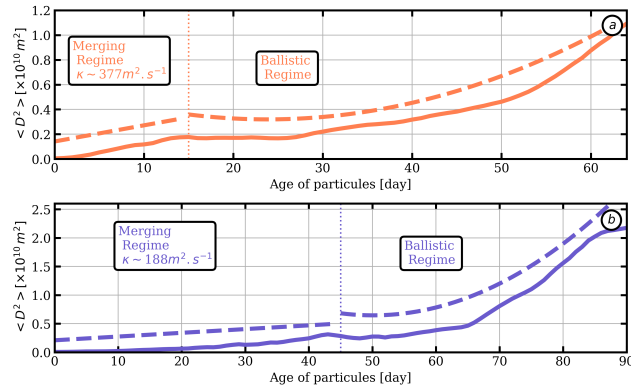
Figure 10. (a) and (b) time evolution of the mean square distance between particles and their center of mass regarding the submesoscale cyclone and anticyclone respectively.
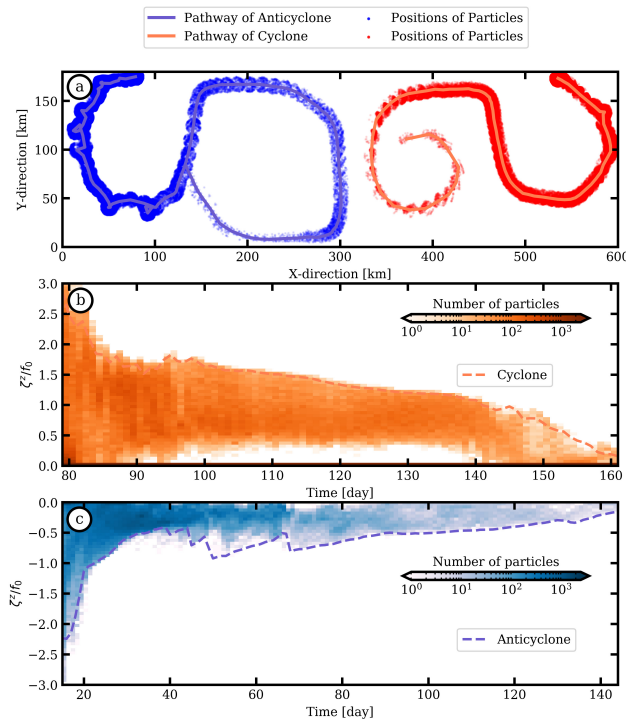

Figure 11. (a) Trajectories of the small vortices considered in Figure 8 (orange line) and 9 (blue line) (blue) and positions of particles located at a distance smaller than 8 km from the smaller vortex. (b) and (c) Time evolution of the histogram of vertical relative vorticity normalized by the planetary rotation of particles (colors) and the normalized vertical relative vorticity associated with the small vortices (dashed lines).
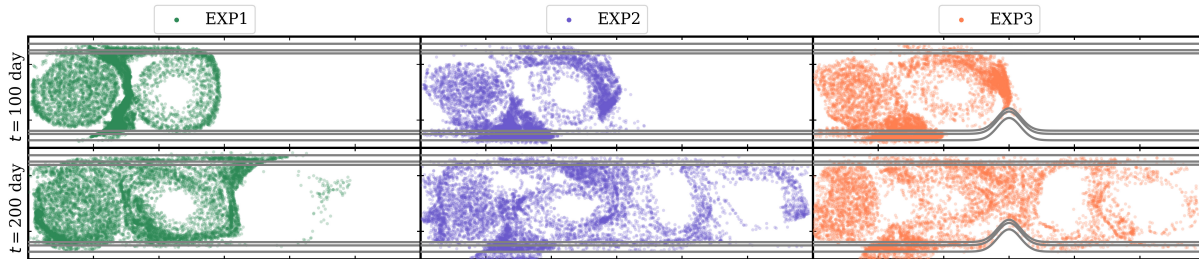
Figure 12. Positions of particles for the three experiments at days 100 and 200.

Probability Density Function (PDF) of the normalized relative vorticity of the selected particles is shown in Figure 11b,c. The normalized relative vorticity associated with the submesoscale eddies dramatically decreases during the very first travel days. This corresponds to the merging events. Indeed, after merger, the submesoscale eddy formed is larger in size but is less intense (note that only potential vorticity is nearly conserved, in the limit of small viscosity). This relative vorticity loss occurs via

5 filamentation and spatial re-organization during the merging process; this re-organization is associated with relative vorticity to vortex stretching conversion, with an increase in potential energy (Ciani et al., 2016). The number of particles trapped in each eddy varies during the merging events. As the submesoscale eddies rotate around their parent mesoscale eddy, they are sheared and they lose particles at their periphery.

10 Finally, the impact of the submesoscale eddy production on the diffusion of particles is highlighted by comparing three experiments (i.e.: EXP1, EXP2 and EXP3). Particles are initially seeded at the southwest edge of the channel between 100 and 300 meter depths. Figure 12 shows the positions of particles with time.

In the EXP1, without BBL vorticity generation (Figure 12, 1st column), particles are advected mostly by mesoscale eddies. Particles remain mostly in the left hand side of the domain. In EXP2 and EXP3 (Figure 12, 2nd and 3rd columns respectively),

15 particles are advected by filaments over the sloping topography, subsequently by submesoscale eddies, and by mesoscale eddy as well. The dispersion of particles is then more efficient in EXP2 and EXP3 than in EXP1.

Following LaCasce (2008), we can estimate a dispersion coefficient as:

$$\kappa = \frac{1}{2}\frac{\mathrm{D}}{\mathrm{D}t} < D^2 > . \tag{14}$$

In Figure 13a, we show the time evolution of the relative dispersion $< D^2 >$ where D is the distance between pairs of

20 particles and $< \bullet >$ is the ensemble average over all the pairs of particles. During the 25 first days of integration, the relative dispersion of particles is similar in the three experiments. Later, the relative dispersion increases more strongly in EXP2 and EXP3. Particles trapped within submesoscale eddies can reach the cyclones and anticyclones on the right side of the domain more easily and travel longer distances. The cape does not play a significant role in the particle dispersion due to the initial configuration of the mesoscale eddies. The estimations of the dispersion coefficient yield $\sim 1000\,\mathrm{m^2s^{-1}}$ in both experiments

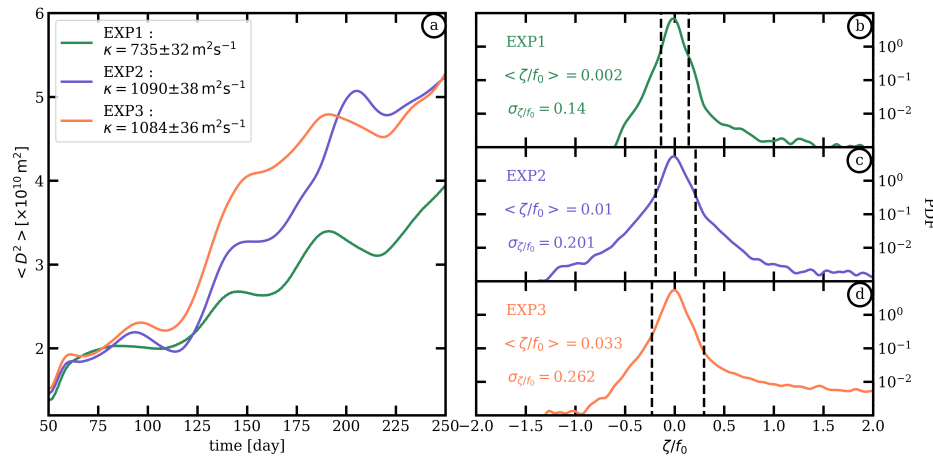25 while in EXP1 it is about $700\,\mathrm{m^2s^{-1}}$.

Ocean Science
Discussions

Figure 13. (a) Time evolution of the dispersion $< D^2 >$ computed for the three experiments: (green) EXP1, (blue) EXP2 and (orange) EXP3. (b) Probability Density Function of the relative vorticity normalized by the planetary rotation associated with particles regarding (green) EXP1, (blue) EXP2 and (orange) EXP3.

In Figure 13b,c,d, we show the PDF of the relative vorticity normalized by the planetary rotation associated with particles at day 200. In the three experiments PDFs are Gaussian shaped and have zero bias, meaning that the influence of cyclonic and anticyclonic motions is similar. However, in EXP2 and EXP3, PDFs flatten and large relative vorticity values are reached (i.e.: $|\zeta^z/f_0| > 0.5$), then the variances increase as a signature of the particle trapping in submesoscale eddies. Finally, particles can

5   also be trapped in the turbulent bottom boundary layer and remain in it for long time. This can be seen in Figure 12 in EXP2 and EXP3 at day 200. There, the bottom boundary layer vorticity is positive and large (i.e.: $|\zeta^z/f_0| > 1.$). That is why, PDF associated with EXP2 and EXP3 show that particles can have very large value of relative vorticity.

Finally, in Figure 14, we compare the number of particles transferred from the left to the right hand side of the channel. In EXP2 and EXP3, the amount of particles lying in the right hand side of the channel is $\sim 15\%$ of the total number of particles.

10   This amount of particles decreases to $\sim 5\%$ in EXP1. This result highlights the impact of submesoscale eddies on the path and spread of particles. Without subsurface submesoscale eddy generation, the fate of particles is driven by the mesoscale eddy field. In this case, particles are trapped in mesoscale eddies or recirculate at the periphery of mesoscale eddies. However, with the subsurface submesoscale eddy generation, particles can be trapped and advected by submesoscale eddies. Then, they can travel over large distance and long time. In EXP2, the amount of particles oscillates through time as a result of the recirculation

15   of particles due to the mesoscale cyclone lying in $x \in [300, 400] \, \mathrm{km}$. These oscillations do not appear in EXP3 which means that the cape does not allow particles to recirculate.
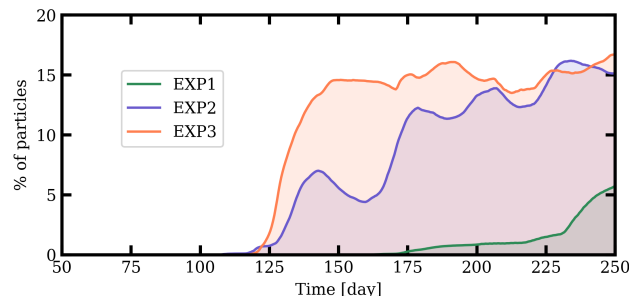
Ocean Science
Discussions

Figure 14. Time evolution of the percentage of particles lying in $x \in [400; 600]$km the three experiments: (green) EXP1, (blue) EXP2 and (orange) EXP3.

4 Conclusions

In situ observations have shown filaments and small eddies of Persian Gulf Water, formed from its outflow along the continental slope of the Gulf of Oman. At this time, a row of alternate signed mesoscale eddies was present in the gulf. We ~~simulated~~ *simulated* numerically an idealized version of this configuration, corresponding to the interaction of a row of surface intensified mesoscale

5   eddies with two topographic slopes in a zonal channel. We used a high-resolution primitive equation model (a 3D hydrostatic model) and showed that the friction of these vortices on the slope (in a slanted bottom boundary layer) is the primary mechanism for the generation of opposite-signed relative vorticity on the slope. The vorticity filaments thus created then undergo shear instability and form a line of small eddies. These small eddies merge and grow in size. They also pair (cyclones with anticyclones) and propagate away from their region of formation. At the surface, these small eddies have a signature and can thus

10   be detected via satellite altimetry. This is due to their strong intensity and to the shallow depth at which they lie. Also, TRW breaking creates turbulence at depth. TRW propagate in the same (opposite) direction as the velocity field at the associated with the mesoscale cyclone (anticyclone). TRW destabilizes *via* baroclinic instability as the velocity of the flow is opposite to its phase speed.

15   The trajectory of submesoscale vortices is often curved and their advection by the mesoscale eddy flow brings these small eddies back towards the topographic slope. There, these eddies generate smaller eddies in turn. This is manifested by a shallower slope of the enstrophy spectrum (more energetic small scales of vorticity). Finally, these small eddies can be destroyed by the shear of the mesoscale eddies (or be incorporated into them) or crash onto the topographic slope and be eroded there. Their lifetime is usually shorter than $3\,\mathrm{months}$ and the length of their pathway is at most $600\,\mathrm{km}$.

20   We have also shown that these small eddies play a non negligible role in the transport and dispersion of tracers (which can be salinity in the Gulf of Oman) by comparing two simulations with and without the BBL vorticity generation. ~~Thanks to~~ *Due to* submesoscale eddies, particles can travel over large distance more rapidly. Finally, the presence of a cape, such as the Cape of

Ra's al Hamra in the Gulf of Oman, does not impact significantly the diffusion of a passive tracer modeling the PGW.

This study also raises other worthwhile questions.

~~More points are worth investigating.~~ In particular, we wish to use a non hydrostatic model to study ~~in more detail~~ *in greater detail* the inter-

action between two SCVs or between one SCV and one mesoscale eddy. ~~The vertical motions created then are of importance~~

~~to the uplift of nutrients in the ocean and to the onset of algae blooms.~~

Few filaments and eddies are observed in our simulation while no realistic surface forcings were implemented; in the ocean,

filaments and small eddies can also originate from the turbulent interaction of eddies or from the instability of upwelling fronts.

The vertical interaction between surface and subsurface SCVs is another ~~offspring~~ *offshoot* of the present study.

The larger upwelling of nutrients in such a study will be important for onset of algal blooms.

Our simulations were done without any surface forcing and generated fewer filaments and eddies. In the real ocean filaments and eddies arise at a range of scales due to turbulent interactions and from instability of upwelling fronts. The interactions between surface and subsurface SCVs in the vertical is another aspect that needs further study.

Ocean Science

Discussions

EGU

Open Access

References

Al Saafani, M., Shenoi, S., Shankar, D., Aparna, M., Kurian, J., Durand, F., and Vinayachandran, P.: Westward movement of eddies into the Gulf of Aden from the Arabian Sea, Journal of Geophysical Research: Oceans, 112, 2007.

Blanke, B. and Raynaud, S.: Kinematics of the Pacific equatorial undercurrent: An Eulerian and Lagrangian approach from GCM results, Journal of Physical Oceanography, 27, 1038–1053, 1997.

Bosse, A., Testor, P., Mortier, L., Prieur, L., Taillandier, V., d'Ortenzio, F., and Coppola, L.: Spreading of Levantine Intermediate Waters by submesoscale coherent vortices in the northwestern Mediterranean Sea as observed with gliders, Journal of Geophysical Research: Oceans, 120, 1599–1622, 2015.

Bower, A. S. and Furey, H. H.: Mesoscale eddies in the Gulf of Aden and their impact on the spreading of Red Sea Outflow Water, Progress in Oceanography, 96, 14–39, 2012.

Bower, A. S., Fratantoni, D. M., Johns, W. E., and Peters, H.: Gulf of Aden eddies and their impact on Red Sea Water, Geophysical Research Letters, 29, 2002.

Capet, X., McWilliams, J. C., Molemaker, M. J., and Shchepetkin, A.: Mesoscale to submesoscale transition in the California Current System. Part I: Flow structure, eddy flux, and observational tests, Journal of physical oceanography, 38, 29–43, 2008a.

Capet, X., McWilliams, J. C., Molemaker, M. J., and Shchepetkin, A.: Mesoscale to submesoscale transition in the California Current System. Part II: Frontal processes, Journal of Physical Oceanography, 38, 44–64, 2008b.

Capet, X., McWilliams, J. C., Molemaker, M. J., and Shchepetkin, A.: Mesoscale to submesoscale transition in the California Current System. Part III: Energy balance and flux, Journal of Physical Oceanography, 38, 2256–2269, 2008c.

Carton, X.: Hydrodynamical modeling of oceanic vortices, Surveys in Geophysics, 22, 179–263, 2001.

Carton, X., L'Hegaret, P., and Baraille, R.: Mesoscale variability of water masses in the Arabian Sea as revealed by ARGO floats, Ocean Science, 8, 227–248, 2012.

Chelton, D. B., Deszoeke, R. A., Schlax, M. G., El Naggar, K., and Siwertz, N.: Geographical variability of the first baroclinic Rossby radius of deformation, Journal of Physical Oceanography, 28, 433–460, 1998.

Ciani, D., Carton, X., and Verron, J.: On the merger of subsurface isolated vortices, Geophysical & Astrophysical Fluid Dynamics, 110, 23–49, 2016.

Cushman-Roisin, B. and Beckers, J.-M.: Introduction to geophysical fluid dynamics: physical and numerical aspects, vol. 101, Academic press, 2011.

D'Asaro, E. A.: Generation of submesoscale vortices: A new mechanism, Journal of Geophysical Research: Oceans, 93, 6685–6693, 1988.

Ferrari, R. and Wunsch, C.: Ocean circulation kinetic energy: Reservoirs, sources, and sinks, Annual Review of Fluid Mechanics, 41, 2009.

Gula, J., Molemaker, M., and McWilliams, J.: Topographic vorticity generation, submesoscale instability and vortex street formation in the Gulf Stream, Geophysical Research Letters, 42, 4054–4062, 2015.

Gula, J., Molemaker, M. J., and McWilliams, J. C.: Topographic generation of submesoscale centrifugal instability and energy dissipation, Nature communications, 7, 12 811, 2016.

LaCasce, J.: Statistics from Lagrangian observations, Progress in Oceanography, 77, 1–29, 2008.

LaCasce, J. and Bower, A.: Relative dispersion in the subsurface North Atlantic, Journal of marine research, 58, 863–894, 2000.

Large, W. G., McWilliams, J. C., and Doney, S. C.: Oceanic vertical mixing: A review and a model with a nonlocal boundary layer parameterization, Reviews of Geophysics, 32, 363–403, 1994.

L'Hégaret, P., Lacour, L., Carton, X., Roullet, G., Baraille, R., and Corréard, S.: A seasonal dipolar eddy near Ras Al Hamra (Sea of Oman), Ocean Dynamics, 63, 633–659, 2013.

L'Hégaret, P., Duarte, R., Carton, X., Vic, C., Ciani, D., Baraille, R., and Corréard, S.: Mesoscale variability in the Arabian Sea from HYCOM model results and observations: impact on the Persian Gulf Water path, Ocean Science, 11, 667, 2015.

5 McWilliams, J. C.: Submesoscale, coherent vortices in the ocean, Reviews of Geophysics, 23, 165–182, 1985.

McWilliams, J. C.: Submesoscale currents in the ocean, Proc. R. Soc. A, 472, 20160 117, 2016.

Molemaker, M. J., McWilliams, J. C., and Dewar, W. K.: Submesoscale instability and generation of mesoscale anticyclones near a separation of the California Undercurrent, Journal of Physical Oceanography, 45, 613–629, 2015.

Pous, S., Carton, X., and Lazure, P.: Hydrology and circulation in the Strait of Hormuz and the Gulf of Oman—Results from the GOGP99

10   Experiment: 1. Strait of Hormuz, Journal of Geophysical Research: Oceans, 109, 2004a.

Pous, S., Carton, X., and Lazure, P.: Hydrology and circulation in the Strait of Hormuz and the Gulf of Oman—Results from the GOGP99 Experiment: 2. Gulf of Oman, Journal of Geophysical Research: Oceans, 109, 2004b.

Prants, S., Budyansky, M., Ponomarev, V., and Uleysky, M. Y.: Lagrangian study of transport and mixing in a mesoscale eddy street, Ocean modelling, 38, 114–125, 2011.

15 Vic, C., Roullet, G., Carton, X., and Capet, X.: Mesoscale dynamics in the Arabian Sea and a focus on the Great Whirl life cycle: A numerical investigation using ROMS, Journal of Geophysical Research: Oceans, 119, 6422–6443, 2014.

Vic, C., Roullet, G., Capet, X., Carton, X., Molemaker, M. J., and Gula, J.: Eddy-topography interactions and the fate of the Persian Gulf Outflow, Journal of Geophysical Research: Oceans, 120, 6700–6717, 2015.